Energy & Environmental Science

Accepted Manuscript

ROYAL SOCIETY OF CHEMISTRY

www.rsc.org/ees

Silolothiophene-Linked Triphenylamines as Stable Hole Transporting Materials for High Efficiency Perovskite Solar Cells

Antonio Abate,*[1] Sanghyun Paek,[2,5] Fabrizio Giordano,[1] Juan-Pablo Correa-Baena,[3] Michael Saliba,[2] Peng Gao,[2] Taisuke Matsui,[4] Jaejung Ko,*[5] Shaik M. Zakeeruddin,[1] Klaus H. Dahmen,[6] Ulf Anders Hagfeldt,[3] Michael Grätzel,[1] Mohammad Khaja Nazeeruddin*[2]

[1] Laboratory for Photonics and Interfaces, Institute of Chemical Sciences and Engineering, École Polytechnique Fédérale de Lausanne, CH-1015-Lausanne, Switzerland.

[2]Group for Molecular Engineering of Functional Materials, Institute of Chemical Sciences and Engineering, École Polytechnique Fédérale de Lausanne, CH-1015-Lausanne, Switzerland

[3]Laboratory of Photomolecular Science, Institute of Chemical Sciences and Engineering, École Polytechnique Fédérale de Lausanne, CH-1015-Lausanne, Switzerland.

[4]Advanced Research Division, Materials Research Laboratory, Panasonic Corporation
1006 Kadoma, Kadoma City, Osaka 571-8501, Japan

[5]Department of Advanced Material Chemistry, Korea University, 2511, Sejong-ro, Sejong City 339-700 (Republic of Korea)

[6]Qatar Environment and Energy Research Institute, a center of Qatar Foundation for Education, Qatar.

* Corresponding authors: AA antonioabate83@gmail.com; JK jko@korea.ac.kr, MKN mdkhaja.nazzeruddin@epfl.ch.

KEYWORDS: perovskite solar cells, device stability, hole transporting materials, photovoltaic, ageing test, hysteresis, maximum power output tracking, glass transition, thermal stability.

ABSTRACT

In this work, we synthesized novel hole transporting materials (HTMs) and we studied their impact on the stability of perovskite-based solar cells (PSCs). The steady-state maximum power output of devices in working condition was monitored to assess the stability and to predict the lifetime of PSCs prepared with different HTMs. We showed that the HTM has significant impact on the device lifetime and we found that novel silolothiophene linked methoxy triphenylamines (Si-OMeTPA) enable more stable PSCs. We reported Si-OMeTPA based devices with half-life of 6 Khrs, compared to 1 Khrs collected for the state-of-the-art PSCs using spirofluorene linked methoxy triphenylamines (spiro-OMeTAD) as HTM. We demonstrated that such clear improvement is correlated to the superior thermal stability of silolothiophene compared to the spiro linked triphenylamines HTMs.

INTRODUCTION

Organic-inorganic perovskites are quickly leading to research activities in new materials for cost-effective and high-efficiency photovoltaic technologies. Since the first demonstration from Kojima and co-workers in 2009,[1] several perovskite-based solar cells (PSCs) have been reported and certified with rapidly improving maximum power conversion efficiency (PCE).[2-4] The recent 20% PCE barrier breaking proved that these materials can compete with long-established inorganic photovoltaics, such as silicon, cadmium telluride and copper indium gallium selenide.[5, 6] In addition, more similar to organic photovoltaics, perovskites allow preparing solar cells from solution processing, which is particularly desired to deliver a low-cost technology.[7]

Compared to such impressive progresses in PCE, the knowledge on device stability in working condition is rather limited. The PCE may drop quite rapidly due to degradation of different device components, such as the perovskite itself and the TiO_2 or organic semiconductors, which are most commonly used as electron and hole selective contacts, respectively.[8-11] Water molecules from the atmosphere are one of the main sources of degradation for the perovskite,[12] but it can be avoided by processing and testing the devices in inert gas or dry air. Leijtens, Pathak and co-workers demonstrated that the TiO_2 can also cause a drop in performance if devices are exposed to UV-light in oxygen-free conditions, such as when the active layer is sealed between two glasses.[13, 14] However, they showed that doping the TiO_2 with aluminium or simply filtering the UV component of the solar spectrum is sufficient to retard this degradation mechanism. More recently a number of studies indicated that the hole transporting materials (HTMs) can play a key role in controlling the long-term stability of PSCs. In particular, Mei, Li, Habisreutinger and co-workers demonstrated that PSCs are more stable if the organic semiconductors are replaced by carbon nanotubes as HTMs.[15, 16] Furthermore, Liu and co-workers showed that employing dopant-free organic HTMs significantly improves the device stability compared to the commonly used chemical doping.[17-20] Previous studies provided

valuable indications on potential degradation mechanisms. Nevertheless it is still problematic to predict the lifetime of PSCs in working condition. There is an intrinsic complication, which stems from the fact that any small difference in the device architecture, preparation procedures and materials composition strongly affects the stability of PSCs. In addition, stability tests are difficult to compare since they have often been performed at different temperature, illumination, such as with or without UV-light filtering, and atmosphere conditions, such as humid or dry air and inert gases. Finally, device performance has been mostly monitored by regularly collecting current-voltage (JV) characteristics during the ageing, as it was established in protocols used for silicon solar cells.[21] However, the JV characteristic of PSCs may show relatively large hysteretic behaviour, which makes it ambiguous to estimate the actual PCE.[22, 23] In freshly made devices this problem can be minimized by slowing down the voltage sweep rate,[23] but for aged devices Tress and co-workers recently showed that even if the hysteresis of the JV scan has almost vanished, the steady-state photocurrent and thus the actual PCE can be significantly lower.[24]

In this work, we study the stability of PSCs using novel HTMs under working condition in inert gas and UV-filtered sunlight. We propose a testing protocol to extract reliable and reproducible ageing data, which enables predicting the device lifetime. We show that a slow and long lasting component of the degradation dynamic is correlated to the stability of the HTM and we demonstrate that new silolothiophene linked methoxy triphenylamines (Si-OMeTPA) significant enhances the lifetime of state-of-the-art PSCs prepared with spirofluorene linked methoxy triphenylamines (spiro-OMeTAD).

RESULTS AND DISCUSSION

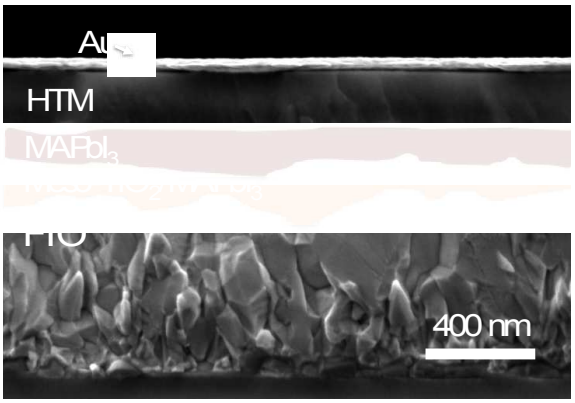

Figure 1. Cross-sectional SEM image of PSCs prepared in this work. From the bottom we see a fluorine doped tin oxide (FTO) layer, mesoporous TiO_2 infiltrated with methylammonium lead iodide perovskite ($MAPbI_3$), capping layer of $MAPbI_3$, the HTM layer and the top gold (Au) electrode.

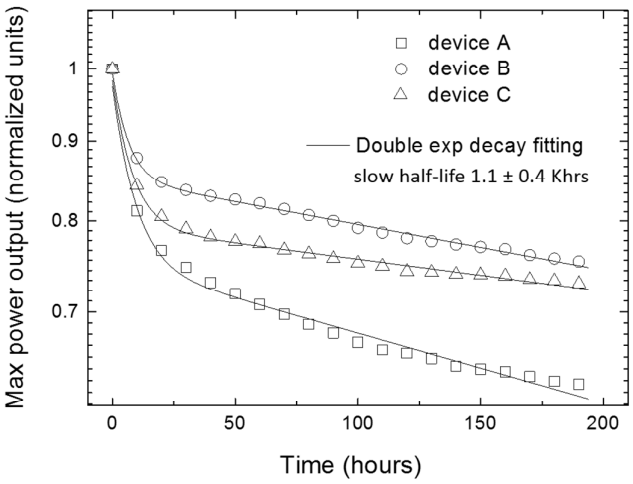

Figure 2. Maximum power output tracking of three identical perovskite solar cells prepared using spiro-OMeTAD as hole transporting material and mesoporous TiO_2 as electron collecting layer. The measurement was performed under UV-filtered simulated sun light in argon atmosphere. Device temperature reached 45°C after a few minutes of light exposure. During the measurement the applied voltage was automatically adjusted to continuously keep the devices at the maximum power point as described in the Experimental Section. The power conversion efficiency at time zero was measured after taking the devices in argon and dark for 24 hours and it was between 14% and 15% for all the devices. Experimental data were fitted to a double exponential decay function (see fitting parameters in Supporting Information) reproduced by the solid lines in figure. The half-life constant of the slow decay component was reported in the graph as averaged over devices A, B and C.

The cross-sectional view of PSCs prepared in this work is shown in Figure 1 by high resolution scanning electron microscopy. From the bottom we can identify the FTO glass with compact TiO_2, a mixed mesoporous TiO_2 and perovskite crystals, a perovskite crystal capping layer, the HTM and the gold electrode. To study the performance degradation of PSCs in working condition, we monitored the steady-state maximum power output (MPO) over several days of testing. During the measurement, devices were kept constantly under UV-filtered simulated sunlight and forward bias voltage. The applied voltage was automatically adjusted to continuously keep the devices at the maximum power point. In Figure 2, we report the MPO decay of three identical devices (A, B and C) made by a facile, solution-processed perovskite on mesoporous TiO_2 and using chemical doped spiro-OMeTAD as HTM.[17, 25] Devices were prepared and tested in inert gas conditions following the procedure described in the Experimental Section. The MPO traces of devices A, B and C in Figure 2 show an early rapid decay that affects the MPO in the first testing hours and a second slower decay that becomes dominant at longer time exposures. The experimental data accurately fit a double exponential decay function, which allows extracting two half-life constants (see Supporting Information). In the first few hours the MPO drops with a fast half-life of 5.3 hrs, as averaged on three devices reported in Figure 2. Similar dynamics have been recently observed by Guarnera and co-workers, which demonstrated that a rapid degradation mechanism is activated by metal electrode migration through the spiro-OMeTAD and contacting the perovskite layer.[26] A direct contact between the metal and the perovskite results in detrimental electronic shunt pathways, which lower the MPO. Though this degradation mechanism is relatively rapid, it saturates in a few hours and thus impacts only marginally the long-term stability.[26]

After few hours of ageing the MPO goes into the second degradation regime which exhibits a slow half-life of 1100 hours, as averaged on three devices reported in Figure 2. This large difference between the first fast and the second slow exponential decay suggests a new

degradation mechanism that becomes dominant after few hours of device functioning. Though the new degradation regime is significantly slower than the first, it nevertheless does not saturate and thus it may dramatically impact the long-term stability. This degradation could in principle be correlated to any of the device components, such as the perovskite, the TiO_2 and the spiro-OMeTAD, or a complex combination of them. However, we prepared and tested devices in inert gas and UV-filtered light condition, which should guarantee relatively stable TiO_2 and perovskite over the testing time.[13] Therefore, we postulated that the degradation of HTM contributes to this slow and long lasting MPO decay and we compared different HTMs to demonstrate this theory.

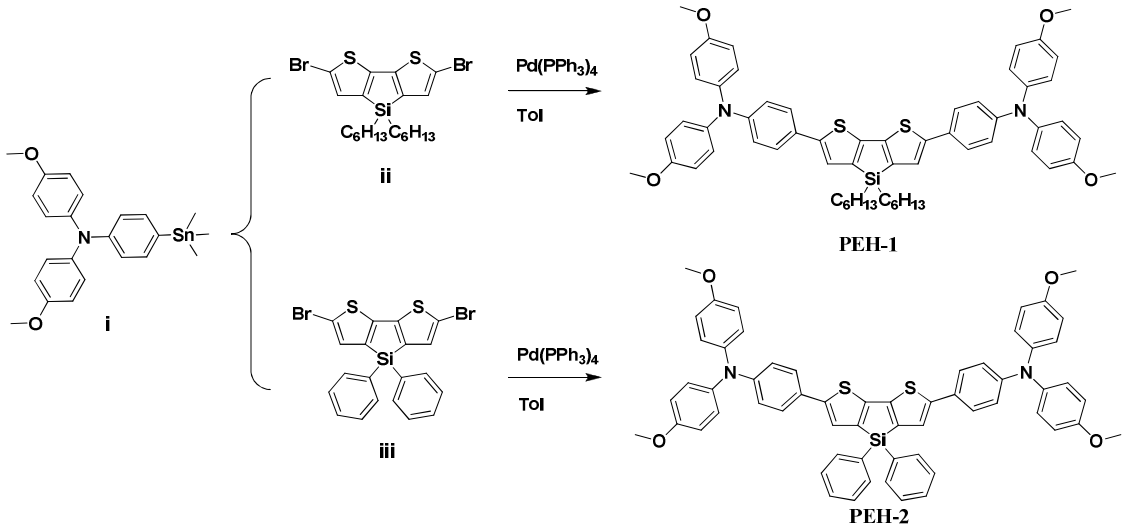

Scheme 1. Schematic diagram of the synthetic procedures used to prepare two OMeTPA-Si derivatives**, PEH-1** and **PEH-2**. A detailed description of all the synthetic steps is given in the Experimental Section.

We prepared new silolothiophene linked methoxy triphenylamine (Si-OMeTPA) derivatives using the synthetic protocol shown in Scheme 1. 4-methoxy-*N*-(4-methoxyphenyl)-*N*-(4-(trimethylstann-yl)phenyl)aniline (**i**) was prepared by *n*-BuLi followed by reaction with trimethyltin chloride. Dibromo-substituted compound **ii** and **iii** were prepared by bromination with NBS in DMF.[27] The Stille reaction[27] of **ii** and **iii** with 2.5 equivalents of **i** in toluene produced two Si-OMeTPA**, PEH-1** and **PEH-2**. Additional details are given in the Experimental Section.

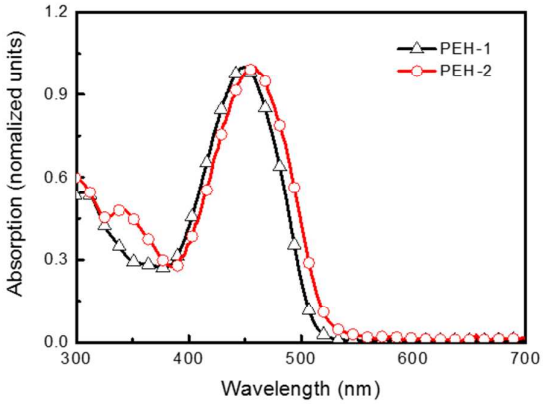

Figure 3. UV-Vis absorption spectra of the **PEH-1** and **PEH-2** in dichloromethane.

In Figure 3 we report the absorption spectra of **PEH-1** and **PEH-2** in dichloromethane. Both the Si-OMeTPA derivatives showed similar spectra with a broad absorption in the ultraviolet region and a strong absorption band in the visible region. The latter peak around 450 nm with the **PEH-2** trace was red shifted compared to **PEH-1**. This shift suggests that the benzyl groups attached to sp^3 silicon in **PEH-2** stabilizes more effectively the first molecular excited state compared to the alkyl chains functionalized silicon in **PEH-1**.[28]

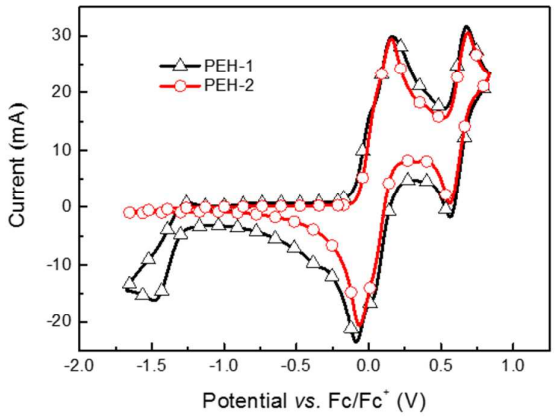

Figure 4. Cyclic voltammogram traces of **PEH-1** and **PEH-2** in dichloromethane, with 0.1 M tetrabutylammonium hexafluorophosphate, scan speed 100 mV s^{-1}, potentials *vs.* Fc/Fc^{+}.

Table 1. Electrochemical parameters extracted from data in Figure 3 and 4.

	$E_{0\text{-}0}$ (eV)[a]	E^{0}_{ox} (V)[b]	E_{HOMO} (eV)[c]	E_{LUMO} (eV)[d]
PEH-1	2.43	0.035	-5.16	-2.73
PEH-2	2.37	0.045	-5.17	-2.80

[a] Zero-zero transition ($E_{0\text{-}0}$) was estimated from the threshold of the absorption spectra in dichloromethane. [b] Redox potential (E^{0}_{ox}) was measured *vs.* Fc/Fc^{+} in dichloromethane with 0.1 M tetrabutylammonium hexafluorophosphate, scan rate of 100 mVs^{-1}. [c] The energy of the highest occupied molecular orbital (E_{HOMO}) was calculated as E^{0}_{ox} (V) *vs.* Fc/Fc^{+} + 0.69 *vs.* NHE + 4.44 *vs.* Vacuum. [d] The energy of the lowest unoccupied molecular orbital (E_{LUMO}) was calculated as $E_{0\text{-}0} - E_{ox.}$

In Figure 4 we report the cyclic voltammogram traces of **PEH-1** and **PEH-2** in dichloromethane. Both Si-OMeTPA derivatives show evidence of two oxidation peaks, which are rather similar since they correspond to one electron oxidation process for the same electron donating triphenylamine units.[29] We converted the oxidation potentials (E^{0}_{ox}) to the energy of the highest occupied molecular orbital (E_{HOMO}) by following the procedure previously described.[30] We estimated the zero-zero transition ($E_{0\text{-}0}$) from the threshold of the absorption spectra in dichloromethane (see Figure 3) and used this value to calculate the energy of the lowest unoccupied molecular orbital (E_{LUMO}). All optoelectronic properties are summarized in Table 1.

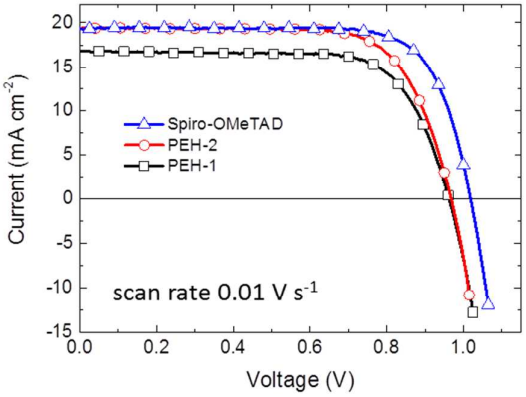

Figure 5. Current-voltage curves of the solar cells collected under AM1.5 simulated sun light. Devices were masked with a metal aperture of 0.16 cm^2 to define the active area. The curves were recorded scanning at 0.01 V s^{-1} from forward bias to short circuit condition.

Table 2. Solar cell performance parameters: short circuit photocurrent (J_{sc}), power conversion efficiency (PCE), open circuit voltage (V_{oc}), fill factor (FF) and series resistances (R_s), as extracted by fitting the current-voltage curves in Figure 5 to an ideal diode model.

	J_{sc} (mA cm^{-2})	V_{oc} (V)	FF	R_s (Ohm cm^{-2})	PCE (%)	Light intensity (mW cm^{-2})
Spiro-OMeTAD	19.4	1.02	0.76	44	15.2	98.0
PEH-2	19.4	0.97	0.72	87	13.5	99.9
PEH-1	16.8	0.96	0.72	103	11.7	100.0

We prepared PSCs using the new molecules as HTMs with the usual doping composition as detailed in the Experimental Section.[17, 25] In Figure 5 we report the JV characteristics of PSCs prepared with Si-OMeTPA derivatives and spiro-OMeTAD. In Table 2, we summarize the device performance parameters, as extracted from the JV curves in Figure 3, and the light intensity measured right before each JV scan. We note that **PEH-2** allowed collecting nearly identical short circuit current (J_{sc}) to spiro-OMeTAD, while the J_{sc} for the **PEH-1** device was over 2.5 mA cm^{-2} lower. Both the Si-OMeTPA devices showed a similar open circuit voltage (V_{oc}), which was about 50 mV lower than that of spiro-OMeTAD. This can be rationalized considering that the E_{HOMO} we measured for both Si-OMeTPA derivatives were about 50 meV higher than the value reported for the spiro-OMeTAD (-5.22 eV).[31] From the fitting of the JV

curves in Figure 2 we extracted the device series resistance (R_s). The R_s values reported in Table 1 showed that the Si-OMeTPA devices have higher R_s than spiro-OMeTAD, which contributes to the lower fill factor (FF). The calculated PCEs are 15.2, 13.5 and 11.7% for spiro-OMeTAD, **PEH-2** and **PEH-1** respectively.

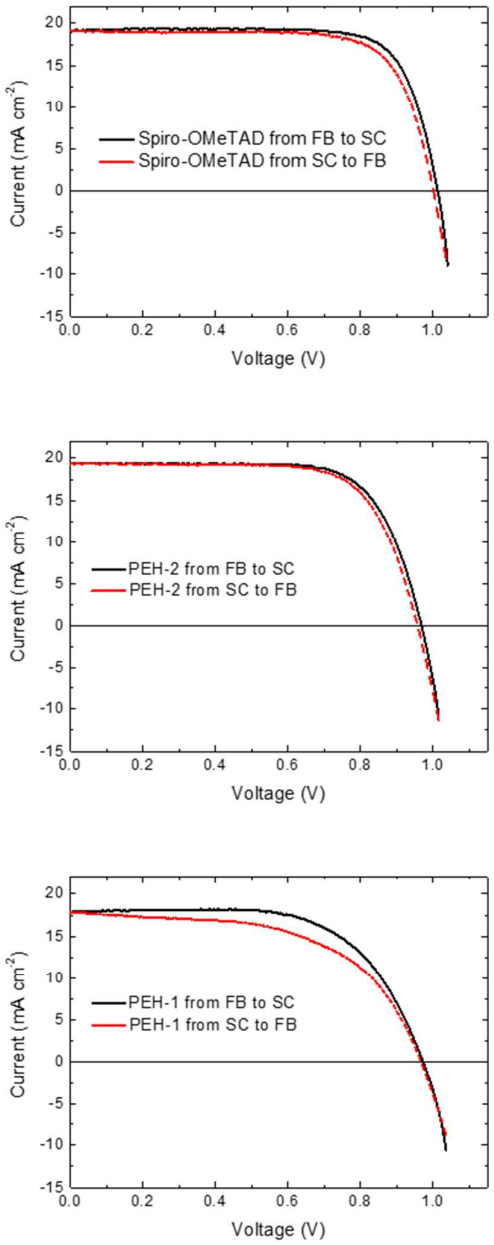

Figure 6. Current-voltage curves of the solar cells collected under AM1.5 simulated sun light. Devices were masked with a metal aperture of 0.16 cm^2 to define the active area. The curves were recorded scanning at 0.01 V s^{-1} from forward bias (FB) to short circuit condition (SC) and the other way around.

Table 3. Solar cell performance parameters: short circuit photocurrent (J_{sc}), power conversion efficiency (PCE), open circuit voltage (V_{oc}), fill factor (FF) extracted from the data in Figure 6.

	Scan direction	*J_{sc} (mA cm^{-2})*	*V_{oc} (V)*	*FF*	*PCE (%)*	*Light intensity (mW cm^{-2})*
Spiro-OMeTAD	FB to SC	19.0	1.01	0.78	15.2	98.4
	SC to FB	19.2	1.00	0.74	14.2	
PEH-2	FB to SC	19.6	0.97	0.68	13.1	98.0
	SC to FB	19.6	0.95	0.66	12.3	
PEH-1	FB to SC	17.9	0.97	0.65	11.5	97.8
	SC to FB	17.8	0.97	0.56	9.7	

We note that the JV characteristic of PSCs may show hysteretic behaviour, which makes it ambiguous to estimate the actual PCE.[22, 23] To show the impact of the hysteresis on our device performances, we reported in Figure 6 the JV traces of PSCs collected by scanning the applied voltage at 0.01 V s^{-1} from forward bias (FB) to short circuit (SC) and the other way around. All the devices have been prepared and tested at the same time, using identical preparation conditions. In Table 3, we summarized the device performance parameters as extracted from both directions of the JV curves reported in Figure 6. It is interesting to note that **PEH-1** showed the lowest J_{sc} and the highest hysteresis, while **PEH-2** and spiro-OMeTAD showed similar hysteretic behaviour.[24]

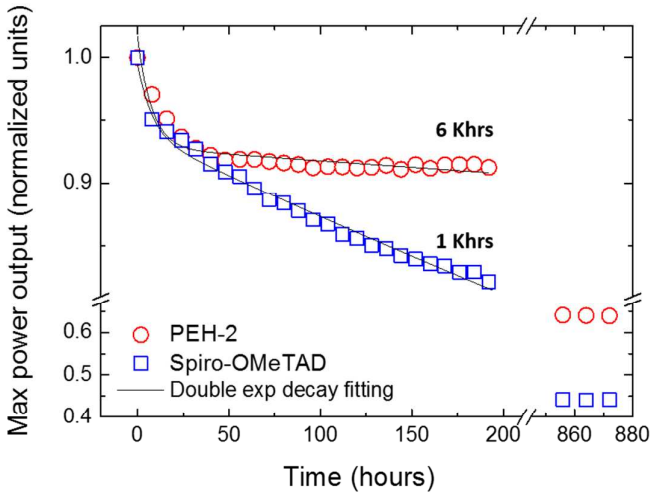

Figure 7. Maximum power point tracking of perovskite solar cells prepared in a single experiment, using **PEH-2** and spiro-OMeTAD as hole transporting materials. The measurement was performed under UV-filtered simulated sun light in argon atmosphere. Device temperature reached 45°C after few minutes of light exposure. The initial power conversion efficiency was measured after storing the device under argon and in the dark for 24 hours and it was over 13 and 14% for **PEH-2** and spiro-OMeTAD respectively. The half-life constants reported in the graph were calculated as reported in Figure 2 with an error of 0.4 Khrs. The maximum power output was monitored for 875 hours taking the device in working condition.

In Figure 7, we report the MPO decay of PSCs prepared in a single experiment, using chemical doped **PEH-2** and spiro-OMeTAD as HTMs. As for data reported in Figure 2, devices were prepared and aged in inert gas condition and under UV-filtered light, following the preparation procedure reported in the Experimental Section. We note that there is no trace for **PEH-1** since devices employing **PEH-1** were extremely unstable, their MPO traces dropped to almost zero within few hours of testing (see Supporting Information). **PEH-1** is an aliphatic substituted Si-compound which are well known to undergo a beta-hydrogen elimination forming an intermediate Si-H complex which will further decompose.[32] The enhanced stability of **PEH-2** is due to prevention of beta elimination caused by replacing alkyl by aryl substitution. As we already observed for a number of devices prepared in different experiments (see Figure 2), the MPO traces of **PEH-2** and spiro-OMeTAD devices reported in Figure 7 showed a double exponential decay trend within the first 200 hours of testing. In particular, they have a very

similar early time decay, which can be well modelled using the same fast half-life (5.3 hrs) calculated by averaging the MPO decays of three different spiro-OMeTAD devices reported in Figure 2. According to the result from Guarnera and co-workers,[26] we assigned this decay to the formation of shunting pathways caused by metal electrode migrating within the HTM and contacting the perovskite layer. The fact that both devices exhibit the same fast half-life constant suggests that this degradation mechanism is active regardless of the particular HTM used. However, it saturates within few hours and thus it will impact only marginally the long-term stability. More significant, the second and longer lasting decay regime shows that the **PEH-2** device degrades with a half-life 6 times larger than that of spiro-OMeTAD. In Figure 7, we also report the MPO collected after 850 hrs, which decay to 0.65 and 0.45 of the initial value for **PEH-2** and spiro-OMeTAD, respectively. We note that in the time window between 200 and 850 hrs the devices were kept under light and inert gas condition, but not always under applied bias voltage. Nevertheless, the MPO after 850 hrs is in good agreement with the trend we found in the first 200 hrs of testing, confirming that the **PEH-2** is substantially more stable than spiro-OMeTAD device. We highlight that data reported in Figure 7 were collected from devices prepared in a single experiment, following the same procedures and using the same chemical doping composition for both the HTMs. Therefore, except for the HTM, there are no differences in the device architecture, preparation procedures and materials composition that can justify such large difference in long-term stability. In addition, both the HTMs have the same triphenylamines donor units, which are linked by silolothiophene or spirofluorene groups in **PEH-2** and spiro-OMeTAD respectively. This apparently minor difference impacted dramatically the device lifetime, demonstrating that the design of the HTM is crucial to prepare stable PSCs. A recent study from Malinauskas and co-workers showed that the thermal stability of the spiro-OMeTAD is the main source of long-term performance degradation in solid-state solar cells.[33] In particular they demonstrated that during the device operational a thermal

transition from an amorphous to a crystalline phase causes morphological changes within the spiro-OMeTAD film that may reduce the mechanical contact of the hole transporting layer with the other device components, thus retarding the charge collection and the overall device performances. We found from thermal gravimetric analysis that **PEH-2** has superior thermal stability than spiro-OMeTAD (see Supporting Information). In particular we found from differential scanning calorimetry (DSC) that the glass transition temperature of **PEH-2** is over 100°C higher than spiro-OMeTAD. A higher glass transition temperature retards the formation of crystalline domains within the hole transporter layer during the device ageing,[33] which results in more stable device performances under working condition. However, for **PEH-1**, the DSC measurement revealed an endothermic transitions around 120°C. This suggests the presence of a crystalline phase at room temperature when the molecule is processed from solution, which is consistent with the rapid degradation observed in the **PEH-1** devices.

CONCLUSIONS

In this work, we synthesized novel HTMs and we studied their stability in PSCs under working condition. Previous studies showed that the stability of PSCs is strongly affected by the device preparation and ageing conditions. Nevertheless, we pointed out that the testing protocol may originate additional inconsistencies. To get more reproducible ageing data, we proposed to monitor the device steady-state maximum power output in working condition. Making use of this method, we estimated that the state-of-the-art PSCs prepared with mesoporous TiO_2 and spiro-OMeTAD have a half-life of about 1 Khrs. To improve the device lifetime we explored new HTMs and we found that particular silolothiophene linked triphenylamines enable preparing PSCs with a half-life of about 6 Khrs. We demonstrated that such clear improvement is correlated to the superior thermal stability of silolothiophene compared to the spiro linked triphenylamines HTMs. This result proved that the HTMs have a strong impact on the long-term stability of PSCs and we expect that further advances, in both stability and power conversion efficiency of PSCs, will come by exploring new silolothiophene derivatives.

EXPERIMENTAL SECTION

General Methods. All the synthetic procedures and the devices fabrication were carried out under nitrogen atmosphere. All reagents and solvents were purchased from commercial sources and used without further purification unless otherwise noted.

Chemical, electrochemical and optoelectronic characterization techniques. ^{1}H and ^{13}C NMR spectra were obtained using a Bruker spectrometer (400 MHz) and Bruker AvanceIII-400 (400MHz) and are reported in ppm using $CDCl_3$-d as an internal standard. Absorption spectral measurements were recorded using JASCO V630 UV–visible spectrophotometer. Thermal analysis was conducted using Sinco TGA N-1000 under nitrogen atmosphere. Cyclic voltammetry was measured with an Autolab Eco Chemie cyclic voltammeter in dichloromethane solvent. The experimental setup consisted of a glassy carbon working electrode, platinum wire counter electrode and platinum reference electrode. Oxygen was removed by bubbling with pure nitrogen gas for 5 min at room temperature. The system was initially calibrated with ferrocene/ferrocenium (Fc/Fc^{+}) redox couple. Redox potential of HTM's measured in CH_2Cl_2 with 0.1 M $(n\text{-}C_4H_9)_4N\text{-}PF_6$ as a scan rate of 100 mV s-1.

Synthetic procedures and chemical characterization. 5,5'-Bis[4-trimethylstannyl-N,N-di(4-methoxyphenyl)aniline]-3,3'-dihexylsilylene-2,2'-bithiophene (**PEH-1**): 4-bromo-N,N-bis(4-methoxyphenyl)aniline (0.55 g, 1.04 mmol) in dry THF under nitrogen atmosphere, was added drop-wise n-BuLi (0.68 ml, 2.5 M in hexane) at -78 ºC. After 30 min stirring at -78 ºC, 1.71 ml of trimethyltin chloride (1.0 M in THF solution) was added slowly to the reaction solution at -78 ºC. The temperature of the solution was warmed to room temperature and the reaction was stirred overnight. Then, the reaction was quenched with brine. The solution was extracted with diethylether, dried with $MgSO_4$. Compound *i* was obtained without any

purification. Compound *i* and *ii* (0.33 g, 0.5 mmol), $Pd(PPh_3)_4$ (0.077 g, 0.067 mmol), and anhydrous toluene (50 ml) were added to a 125 mL flame-dried Schlenk flask with a condenser under a nitrogen atmosphere. The reaction mixture was heated to reflux for 1 day, then cooled it to room temperature. The organic layer was separated and dried over anhydrous $MgSO_4$. The solvent was removed in vacuum overnight. The orange product was purified by column chromatography. Yield: 60 %. MS: m/z 968.4 [M+]. ^{1}H NMR (400 MHz, $CDCl_3$): δ 7.43 (d, J = 8.0 Hz, 4H), 7.17 (S, 2H), 7.13 (d, J = 8 Hz, 8H), 6.95 (d, J = 8.0 Hz, 4H), 6.86 (d, J = 8.0 Hz, 8H), 3.83 (s, 12H), 1.44 (m, 4H), 1.37 (m, 4H), 1.32 (m, 8H), 0.96 (m, 4H), 0.88 (t, 6H). ^{13}C NMR (100 MHz, $CDCl_3$): δ 155.9, 147.8, 147.5, 145.0, 142.4, 140.7, 127.0, 126.5, 126.2, 124.3, 120.8, 114.7, 55.5, 32.9, 31.4, 24.2, 22.6, 14.1, 11.9.

5,5'-Bis[4-trimethylstannyl-N,N-di(4-methoxyphenyl)aniline]-3,3'-diphenylsilylene-2,2'-bithiophene (**PEH-2**) was synthesized following a procedure similar to what we used for **PEH-1**, except that *iii* (0.3 g, 0.59 mmol) was used in place of *ii*. Yield: 65 %. MS: m/z 952.2 [M+]. ^{1}H NMR (400 MHz, $CDCl_3$): δ 7.71 (d, J = 8.0 Hz, 4H), 7.45-7.37 (m, 10H), 7.33 (S, 2H), 7.10 (d, J = 8 Hz, 8H), 6.94 (d, J = 8.0 Hz, 4H), 6.86 (d, J = 8.0 Hz, 8H), 3.83 (s, 12H). ^{13}C NMR (100 MHz, $CDCl_3$): δ 156.1, 148.2, 135.8, 135.4, 134.8, 131.8, 130.3, 128.5, 128.2, 127.8, 127.4, 126.9, 126.6, 120.2, 114.9, 55.5.

Solar cells fabrication. Devices were fabricated on fluorine doped tin oxide (FTO) coated glass substrates. The substrates were cleaned sequentially with Hellmanex in ultrasonic bath for 30 min, then washed with acetone, isopropanol and finally cleaned with oxygen plasma for 5 min. A 30 nm TiO_2 compact layer was deposited on FTO via spray pyrolysis at 450°C from a precursor solution of titanium diisopropoxide bis(acetylacetonate) in anhydrous ethanol. After the spraying, the substrates were left at 450°C for 45 min, then they were left to cool down to room temperature. Mesoporous TiO_2 layer was deposited by spin coating for 20 s at 4000 rpm

with a ramp of 2000 rpm s^{-1}, using 30 nm particle paste (Dyesol) diluted in ethanol to achieve 150 nm thick layer. After the spin coating, the substrate was immediately dried at 100°C for 10 min and then sintered again at 500°C for 30 min, under dry air flow.

Upon cooling to room temperature, the perovskite layer was deposited in a nitrogen-filled glovebox by spin coating the perovskite precursor solution. The latter was prepared dissolving a stoichiometric amount (1:1 molar ratio) of lead iodide and methyl ammonium iodide in dimethylsulfoxide at a concentration of 1.1 M of each component. The spin coating program includes two steps, first 1000 rpm for 10 s with a ramp of 200 rpm s^{-1}, then 6000 rpm for 30 s with a ramp of 2000 rpm s^{-1}. 10 s before the end of the spin-coating program, chlorobenzene was gently dropped on the spinning substrate for 2 s using an automatic dispenser. The substrate was then heated at 90°C for 1 h on a hotplate in the nitrogen-filled glovebox.

The HTMs were subsequently deposited on the top of the perovskite layer by spin coating from solution at 4000 rpm for 20 s with a ramp of 2000 rpm s^{-1}. The HTM solutions were prepared dissolving the compounds (**PEH-1**, **PEH-2** or spiro-OMeTAD) in chlorobenzene at concentration of 60 mM, with the addition of 50 mol% of bis(trifluoromethanesulfonyl)imide (Aldrich) from a stock solution of 1.8 M in acetonitrile), 330 mol% of tert-butylpyridine (Aldrich) and 2 mol% of Tris(2-(1H-pyrazol-1-yl)-4-tert-butylpyridine)- cobalt(III) Tris(bis(trifluoromethylsulfonyl)imide) (Dyesol) from a stock solution 0.25 M in acetonitrile.

Finally, 80 nm of gold was deposited by thermal evaporation under high vacuum, using a shadow masking to pattern the electrodes.

Solar cells characterisation. A ZEISS Merlin HR-SEM was used to characterize the morphology of the device cross-section. Current-voltage characteristics were measured in air under AM 1.5 simulated sunlight with a potentiostat (Keithley). The light intensity was measured for calibration with an NREL certified KG5 filtered Si reference diode. The solar cells

were masked with a metal aperture of 0.16 cm^2 to define the active area. The current-voltage curves were recorded scanning at 0.01 V s^{-1}.

Stability was measured placing devices in a box under 20 mL min^{-1} argon flow. During the test the devices were constantly kept at the maximum power point under 100 mW cm^{-2} light intensity using white LED, with no light emission at wavelengths below 400 nm. The temperature of the testing box stabilized at 45°C after few minutes under light. To keep the device constantly at the maximum power output we used a maximum power point tracking algorithm similar to what recently reported by Ahmed and co-workers.[34]

Thermal characterisations. Differential scanning calorimetry (DSC) was conducted on a DSC8000 calorimeter from PerkinElmer using 2−4 mg of sample powder placed in an aluminium pan with a corresponding tight-fitting lid. The scans were taken from 30°C to 300°C at a rate of 10°C min^{-1} in a nitrogen atmosphere. Thermal gravimetric analysis was conducted using Scinco TGA N-1000 under a nitrogen atmosphere.

Acknowledgment

AA has received funding from the European Union's Seventh Framework Programme for research, technological development and demonstration under grant agreement no 291771. We acknowledge financial support from CTI 15864.2 PFNM-NM, Solaronix, Aubonne, Switzerland, and from the European Union Seventh Framework Programme [FP7/2007-2013] under grant agreement n° 604032 of the MESO project, (FP7/2007-2013) ENERGY.2012.10.2.1; NANOMATCELL, grant agreement no. 308997. We thank EPFL, Centre for Electron Microscopy (CIME), and Manual Tschumi for designing the stability measurements system. AA thanks Dr. Thomas Moehl and Dr. Wolfgang Tress for useful discussions during the manuscript preparation.

References

1. A. Kojima, K. Teshima, Y. Shirai and T. Miyasaka, *Journal of the American Chemical Society*, 2009, **131**, 6050-6051.
2. M. M. Lee, J. Teuscher, T. Miyasaka, T. N. Murakami and H. J. Snaith, *Science*, 2012, **338**, 643-647.
3. N. J. Jeon, J. H. Noh, W. S. Yang, Y. C. Kim, S. Ryu, J. Seo and S. I. Seok, *Nature*, 2015, **517**, 476-480.
4. W. Nie, H. Tsai, R. Asadpour, J.-C. Blancon, A. J. Neukirch, G. Gupta, J. J. Crochet, M. Chhowalla, S. Tretiak and M. A. Alam, *Science*, 2015, **347**, 522-525.
5. M. A. Green, K. Emery, Y. Hishikawa, W. Warta and E. D. Dunlop, *Progress in photovoltaics: research and applications*, 2015, **23**, 1-9.
6. N. R. E. Laboratory, *Best Research-Cell Efficiencies; www.nrel.gov/ncpv/images/efficiency_chart.jpg*.
7. L. Liu, A. Mei, T. Liu, P. Jiang, Y. Sheng, L. Zhang and H. Han, *Journal of the American Chemical Society*, 2015, **137**, 1790-1793.
8. A. Krishna, D. Sabba, H. Li, J. Yin, P. P. Boix, C. Soci, S. G. Mhaisalkar and A. C. Grimsdale, *Chemical Science*, 2014, **5**, 2702-2709.
9. H. Li, K. Fu, A. Hagfeldt, M. Grätzel, S. G. Mhaisalkar and A. C. Grimsdale, *Angewandte Chemie International Edition*, 2014, **53**, 4085-4088.
10. P. Qin, H. Kast, M. K. Nazeeruddin, S. M. Zakeeruddin, A. Mishra, P. Bäuerle and M. Grätzel, *Energy & Environmental Science*, 2014, **7**, 2981-2985.
11. A. Abate, M. Planells, D. J. Hollman, V. Barthi, S. Chand, H. J. Snaith and N. Robertson, *Physical Chemistry Chemical Physics*, 2015, **17**, 2335-2338.
12. J. A. Christians, P. A. Miranda Herrera and P. V. Kamat, *Journal of the American Chemical Society*, 2015, **137**, 1530-1538.
13. T. Leijtens, G. E. Eperon, S. Pathak, A. Abate, M. M. Lee and H. J. Snaith, *Nature communications*, 2013, **4**, 2885.
14. S. K. Pathak, A. Abate, P. Ruckdeschel, B. Roose, K. C. Gödel, Y. Vaynzof, A. Santhala, S. I. Watanabe, D. J. Hollman and N. Noel, *Advanced Functional Materials*, 2014, **24**, 6046-6055.
15. A. Mei, X. Li, L. Liu, Z. Ku, T. Liu, Y. Rong, M. Xu, M. Hu, J. Chen and Y. Yang, *Science*, 2014, **345**, 295-298.
16. S. N. Habisreutinger, T. Leijtens, G. E. Eperon, S. D. Stranks, R. J. Nicholas and H. J. Snaith, *Nano letters*, 2014, **14**, 5561-5568.
17. A. Abate, T. Leijtens, S. Pathak, J. Teuscher, R. Avolio, M. E. Errico, J. Kirkpatrik, J. M. Ball, P. Docampo and I. McPherson, *Physical Chemistry Chemical Physics*, 2013, **15**, 2572-2579.
18. J. Liu, Y. Wu, C. Qin, X. Yang, T. Yasuda, A. Islam, K. Zhang, W. Peng, W. Chen and L. Han, *Energy & Environmental Science*, 2014, **7**, 2963-2967.
19. A. Abate, D. R. Staff, D. J. Hollman, H. J. Snaith and A. B. Walker, *Physical Chemistry Chemical Physics*, 2014, **16**, 1132-1138.
20. F. J. Ramos, M. Ince, M. Urbani, A. Abate, M. Grätzel, S. Ahmad, T. Torres and M. K. Nazeeruddin, *Dalton Transactions*, 2015, **44**, 10847-10851.
21. D. Staebler, R. Crandall and R. Williams, *Applied Physics Letters*, 1981, **39**, 733-735.
22. H. J. Snaith, A. Abate, J. M. Ball, G. E. Eperon, T. Leijtens, N. K. Noel, S. D. Stranks, J. T.-W. Wang, K. Wojciechowski and W. Zhang, *The Journal of Physical Chemistry Letters*, 2014, **5**, 1511-1515.
23. E. Unger, E. Hoke, C. Bailie, W. Nguyen, A. Bowring, T. Heumüller, M. Christoforo and M. McGehee, *Energy & Environmental Science*, 2014, **7**, 3690-3698.

24. W. Tress, N. Marinova, T. Moehl, S. Zakeeruddin, M. K. Nazeeruddin and M. Grätzel, *Energy & Environmental Science*, 2015, **8**, 995-1004.
25. J. Burschka, A. Dualeh, F. Kessler, E. Baranoff, N.-L. Cevey-Ha, C. Yi, M. K. Nazeeruddin and M. Grätzel, *Journal of the American Chemical Society*, 2011, **133**, 18042-18045.
26. S. Guarnera, A. Abate, W. Zhang, J. M. Foster, G. Richardson, A. Petrozza and H. J. Snaith, *The Journal of Physical Chemistry Letters*, 2015, **6**, 432-437.
27. G. Lu, H. Usta, C. Risko, L. Wang, A. Facchetti, M. A. Ratner and T. J. Marks, *Journal of the American Chemical Society*, 2008, **130**, 7670-7685.
28. A. Abate, R. P. Tejada, K. Wojciechowski, J. M. Foster, A. Sadhanala, U. Steiner, H. Snaith, S. Franco and J. Orduna, *Physical Chemistry Chemical Physics*, 2015, Advance Article.
29. M. Planells, A. Abate, D. J. Hollman, S. D. Stranks, V. Bharti, J. Gaur, D. Mohanty, S. Chand, H. J. Snaith and N. Robertson, *Journal of Materials Chemistry A*, 2013, **1**, 6949-6960.
30. N. G. Connelly and W. E. Geiger, *Chemical Reviews*, 1996, **96**, 877-910.
31. N. J. Jeon, H. G. Lee, Y. C. Kim, J. Seo, J. H. Noh, J. Lee and S. I. Seok, *Journal of the American Chemical Society*, 2014, **136**, 7837-7840.
32. D. H. Berry and L. J. Procopio, *Journal of the American Chemical Society*, 1989, **111**, 4099-4100.
33. T. Malinauskas, D. Tomkutė-Lukšienė, R. Sens, M. Daskeviciene, R. Send, H. Wonneberger, V. Jankauskas, I. Bruder and V. Getautis, *ACS applied materials & interfaces,* 2015, **7**, 11107-11116.
34. J. Ahmed and Z. Salam, *Applied Energy*, 2015, **150**, 97-108.